

1 The characteristics of the 2022 Tonga volcanic tsunami in the Pacific Ocean

2 Gui Hu¹, Linlin Li^{1,2}, Zhiyuan Ren³, Kan Zhang¹

3 1. Guangdong Provincial Key Laboratory of Geodynamics and Geohazards, School of Earth Sciences
4 and Engineering, Sun Yat-sen University, Guangzhou, China

5 2. Southern Marine Science and Engineering Guangdong Laboratory (Zhuhai), Zhuhai, China

6 3. Department of Civil and Environmental Engineering, National University of Singapore, Singapore.

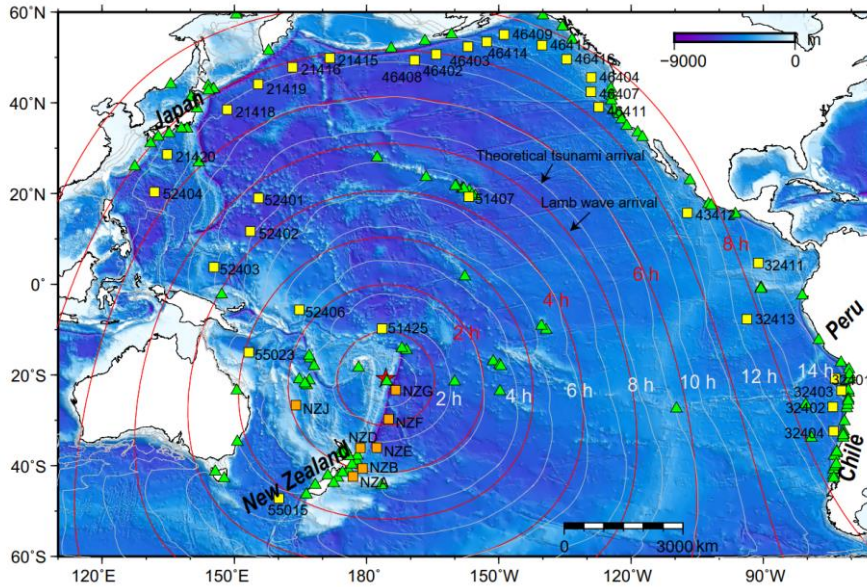
7 *Correspondence to:* Linlin Li (lilinlin3@mail.sysu.edu.cn)

8 **Abstract.** On 15th January 2022, an exceptional eruption of Hunga Tonga–Hunga Ha’apai volcano
9 generated atmospheric and tsunami waves that were widely observed at oceans globally, gaining a
10 remarkable attention to scientists in related fields. The tsunamigenic mechanism of this rare event
11 remains an enigmatic due to its complexity and lacking of direct underwater observations. Here, to
12 explore the tsunamigenic mechanisms of this volcanic tsunami event and its hydrodynamic processes in
13 the Pacific Ocean, we conduct tsunami waveform and spectral analyses of the waveform recordings at
14 116 coastal gauges and 38 deep-ocean buoys across the Pacific Ocean. Combined with the constraints of
15 some representative barometers, we obtain the plausible tsunamigenic origins during the volcano activity.
16 We identify four distinct tsunami wave components generated by air-sea coupling and seafloor crustal
17 deformation. Those tsunami components are differentiated by their different propagating speeds or period
18 bands. The first-arriving tsunami component with ~80–100 min period was from shock waves spreading
19 at a velocity of ~1000 m/s in the vicinity—of the eruption. The second component with extraordinary
20 tsunami amplitude in deep sea was from Lamb waves. The Lamb wave with ~30–40 min period radically
21 propagated outward from the eruption site with spatially decreasing propagation velocities from ~340
22 m/s to ~315m/s. The third component with ~10–30 min period was probably from some atmospheric
23 gravity wave modes propagating faster than 200 m/s but slower than Lamb waves. The last component
24 with ~3–5 min period originated from partial caldera collapse with dimension of ~0.8–1.8 km.
25 Surprisingly, the 2022 Tonga volcanic tsunami produced long oscillation in the Pacific Ocean which is
26 comparable with those of the 2011 Tohoku tsunami. We point out that the long oscillation is not only
27 associated with the resonance effect with the atmospheric acoustic-gravity waves, but more importantly
28 the interactions with local bathymetry. This rare event also calls for more attention to the tsunami hazards
29 produced by atypical tsunamigenic source, e.g., volcanic eruption.

30 **1. Introduction**

31 On 15 January 2022 at 04:14:45 (UTC), a submarine volcano erupted violently at the uninhabited Hunga
32 Tonga-Hunga Ha'apai (HTHH) island at 20.546°S 175.390°W (USGS, 2022). The volcano is located ~67
33 km north of Nuku'alofa, the capital of Tonga (NASA, 2022) (Figure 1). The blasts launched plumes of
34 ash, steam, and gas ~58 km high into stratosphere (Yuen et al., 2022) which not only blanketed nearby
35 islands in ash (Duncombe, 2022; NASA, 2022), but caused various atmospheric acoustic-gravity wave
36 modes (AGWs) of various scales, e.g., Lamb waves from atmospheric surface pressure disturbance
37 associated with the eruption (Liu and Higuera, 2022; Adam, 2022; Kubota et al., 2022; Matoza et al.,
38 2022). Tsunami with conspicuous sea level changes were detected by coastal tide gauges and Deep-ocean
39 Assessment and Reporting of Tsunamis (DART) buoy stations in the Pacific (Figure 1), the Atlantic, and
40 Indian Oceans as well as the Caribbean and Mediterranean seas (Carvajal et al., 2022; Kubota et al., 2022;
41 Ramírez-Herrera et al., 2022), while the large waves were mainly concentrated in the Pacific Ocean, like
42 coastlines of New Zealand, Japan, California, and Chile (Carvajal et al., 2022). The event caused at least
43 3 fatalities in Tonga. Two people drowned in northern Peru when ~2 m destructive tsunami waves
44 inundated an island in the Lambayeque region, Chile (Edmonds, 2022).

45 Satellite images revealed that the elevation of HTHH island has gone through dramatic change before
46 and after the mid-January 2022 eruption. Previously, after the 2015 eruption, the two existing Hunga
47 Tonga and Hunga Ha'apai Islands were linked together. The volcanic island rose 1.8 km from the seafloor
48 where it stretched ~20 km across and topped a underwater caldera ~5 km in diameter (Garvin et al., 2018;
49 NASA, 2022). After the violent explosion on 15 January 2022, the newly formed island during 2015 was
50 completely gone, with only small tips left in far southwestern and northeastern HTHH island (NASA,
51 2022). HTHH volcano lies along the northern part of Tonga–Kermadec arc, where the Pacific Plate
52 subducts under the Indo-Australian Plate (Billen et al., 2003). The convergence rate (15–24 cm/year)
53 between the Tonga–Kermadec subduction system and the Pacific plate is among the fastest recorded plate
54 velocity on Earth, forming the second deepest trench around the globe (Satake, 2010; Bevis et al., 1995).
55 The fast convergence rate contributes to the frequent earthquakes, tsunamis and volcanic eruptions in
56 this region historically (Bevis et al., 1995). The 2022 HTHH volcano is part of a submarine-volcano
57 chain that extends all the way from New Zealand to Fiji (Plank et al., 2020). HTHH volcano had many
58 notable eruptions before 2022 since its first historically recorded eruption in 1912, i.e., in 1937, 1988,



60
 61 **Figure 1. The spatial distribution of the eruption site (red star), DART stations (squares), tide**
 62 **gauges (triangles) and the calculated tsunami arrival times. White contours indicate the modelled**
 63 **arrival times of conventional tsunami. Red contours indicate the estimated arrival times of Lamb**
 64 **waves (see how we derive these contours in section 3.1).**

65 The 2022 HTHH eruption is the first volcanic event which generates worldwide tsunami signatures since
 66 the 1883 Krakatau event (Matoza et al., 2022; Self and Rampino, 1981; Nomanbhoy and Satake, 1995).

67 The tsunamigenic mechanism of this rare volcanic eruption-induced tsunami is still poorly understood
 68 due to its complex nature and the deficiencies of near-field seafloor surveys. Various tsunami generation
 69 mechanisms have been proposed so far based on the observations of ground-based and spaceborne
 70 geophysical instrumentations (Kubota et al., 2022; Matoza et al., 2022; Carvajal et al., 2022). The
 71 mechanisms are closely associated with the air-sea coupling with atmospheric waves. Atmospheric
 72 waves propagating in the atmospheric fluid ~~with different speeds~~ are generated by different physical
 73 mechanisms (Gossard and Hooke, 1975a). Lamb wave is a horizontally propagating acoustic waves
 74 in Lamb mode which is trapped at the earth's surface with group velocities close to the mean
 75 sound velocity of the lower atmosphere (e.g. Lamb, 1932). Atmospheric gravity wave is
 76 triggered when air molecules in the atmosphere are disturbed vertically other than horizontally
 77 (e.g. Le Pichon et al., 2010). Nonlinear propagation of atmospheric wave may cause period

78 ~~lengthening and the formation of shock-wave (Matoza et al., 2022) Nonlinearities in the process~~
79 ~~may lead to the formation of shock wave and period lengthening. The balance between gravity and~~
80 ~~buoyancy causes gravity waves. The acoustic wave propagate by atmospheric fluid compression and~~
81 ~~rarefaction (Matoza et al., 2022).~~ The most-mentioned mechanism of the tsunami is the fast-traveling

带格式的: 字体: (默认) Times New Roman, 字体颜色: 文字 1

82 atmospheric Lamb wave generated by the atmospheric pressure rise of ~2 hPa during the eruption. The
83 Lamb wave circled the Earth for several times with travelling speed close to that of the sound wave in
84 the lower atmosphere, leading to globally observed sea level fluctuations (Adam, 2022; Duncombe, 2022;
85 Kubota et al., 2022; Matoza et al., 2022) (Figure 1). The second mechanism is suggested to be a variety
86 of other acoustic-gravity wave modes (Adam, 2022; Matoza et al., 2022; Themens et al., 2022; Zhang et
87 al., 2022). The third mechanism may be related to the seafloor crustal deformation induced by one or
88 more volcanic activities in the vicinity of the eruption site (e.g., pyroclastic flows, partial collapse of the
89 caldera) (Carvajal et al., 2022) , which are more responsible for the near-field tsunamis with theoretical
90 tsunami speeds.

域代码已更改

91 To investigate the possible tsunamigenic mechanisms and detailed hydrodynamic behaviors of this rare
92 volcanic tsunami event, in this study, we collect, process and analyze the sea level measurements from
93 116 tide gauge and 38 DART buoys in the Pacific Ocean (shown in Figures 1 and 2). We first do statistical
94 analysis of the tsunami waveforms to estimate the propagating speed of the Lamb wave and to understand
95 the tsunami wave characteristics in the Pacific Ocean through demonstrating the tsunami wave properties,
96 i.e., arrival times, wave heights and durations. We then conduct wavelet analysis for representative DART
97 buoys and tide gauges respectively to explore tsunamigenic mechanisms of the event and to better
98 understand its hydrodynamic processes in the Pacific Ocean. Aided by wavelet analysis of corresponding
99 barometers near the selected DART buoys and comparison with tsunami records of the 2011 Tohoku
100 tsunami, we are able to piece together all the analysis and demonstrate that the 2022 HTHH tsunami was
101 generated by air-sea coupling with a wide range of atmospheric waves with different propagating
102 velocities and period bands, and seafloor crustal deformation associated with the volcanic eruption. We
103 demonstrate as well that the tsunami was amplified at the far-field Pacific coastlines where the local
104 bathymetric effects play a dominant role in tsunami scale.

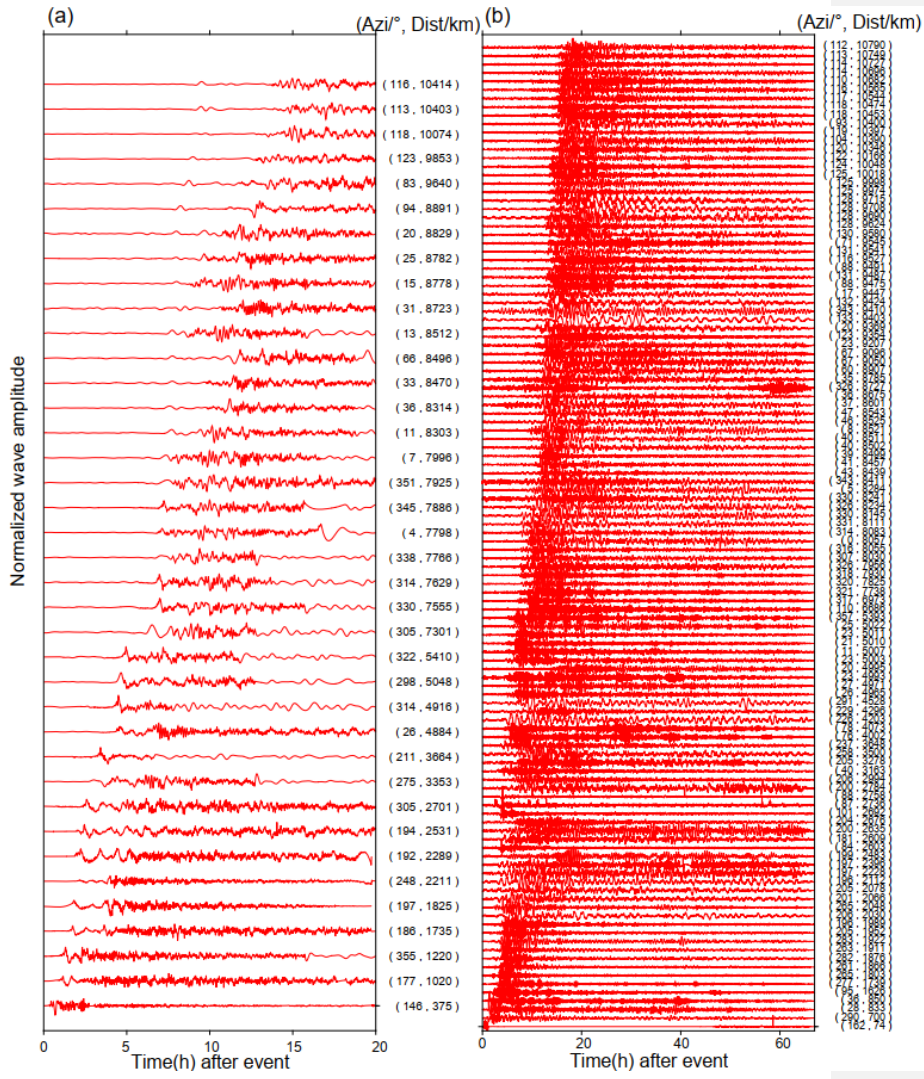
105 **2. Data and Methods**

106 **2.1 Data**

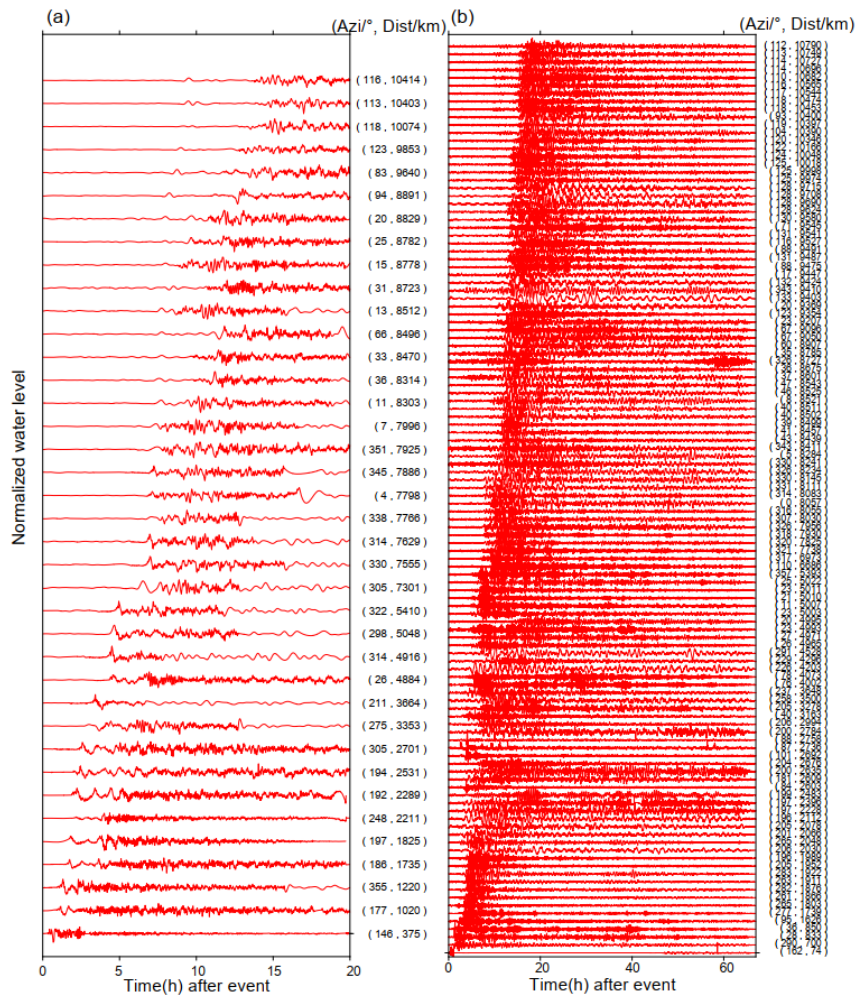
107 We collected high-quality sea level records across the Pacific Ocean at 38 DART buoys (in which 31
108 stations from <https://nctr.pmel.noaa.gov/Dart/>, 7 stations from <https://tilde.geonet.org.nz/dashboard/>) and
109 116 tide gages from IOC (The Intergovernmental Oceanographic Commission, <http://www.ioc-sealevelmonitoring.org>) (Figure 1). The epicentral distances of tide gauges and DART buoys range
110 between 74–10790 km and 375–10414 km, respectively. The sampling rates of DART buoys are
111 changing over time. Passing of tsunami event generally can trigger the DART system to enter its high
112 frequency sampling mode (15 seconds or 1 min) from normal frequency mode (15 min)
113 (www.ndbc.noaa.gov/dart). In contrast, sampling rates of normal tide gauges at coasts are uniform with
114 sampling interval of 1 min. The sampling interval of both DART and tide gauges is preprocessed to 15
115 seconds. Firstly, we eliminate abnormal spikes and fill gaps by linear interpolation. Secondly, we applied
116 a fourth-order Butterworth-Highpass filter with a cut-off frequency of 3.5×10^{-5} Hz (~ 8 hours) to remove
117 the tidal components (Figure 2) (Heidarzadeh and Satake, 2013). After the two steps, quality control step
118 is conducted to select high-quality data, in which we delete waveforms with spoiled data or massive data
119 loss due to equipment failure, or with the maximum tsunami heights of tide gauges less than 0.2 m, then
120 the selected data will be ready for further statistics and spectral analysis. We also collect and analyze the
121 atmospheric pressure disturbance data recorded by some representative barometers. The sampling rates
122 of the barometers is generally uniform with a sampling rate of 1 min except for some stations in New
123 Zealand with interval of 10 min. Considering the sample rate, we employ a fourth-order Butterworth-
124 Bandpass filter with period ranging between 2–150 min for wavelet analysis of the barometers with 1
125 min sample rate, while we apply the fourth-order Butterworth-Bandpass filter with range of 30–150 min
126 to long-period waveform display based on two reasons. (1) The barometer data we use for the analysis
127 include some in New Zealand with 10 min sample rate; (2) Filtering out the short-period waves helps
128 highlight long-period tsunami wave components.

130 The tsunami waveforms recorded by DART buoys which are installed offshore in the deep water are
131 expected to contain certain characteristics of the tsunami source (Wang et al., 2020, 2021). The
132 waveforms recorded by tide gauge distributed along coastlines are significantly influenced by local
133 bathymetry/topography which are used for investigating bathymetric effect on tsunami behaviors

134 (Rabinovich et al., 2017, 2006; Rabinovich, 2009). Therefore, we use the DART data for source-related
 135 analysis and choose some tide gauge data to investigate the tsunami behaviors at the Pacific coastlines.
 136



137



138

139 **Figure 2. Detided tsunami waveforms at (a) DART buoys and (b) tide gauges. Waveforms in both**
 140 **subplots are shown in ascending distance. Azi stands for azimuth. The data are normalized with**
 141 **respect to the largest amplitude of each tide gauge.**

142 **2.2 Tsunami Modelling**

143 We use a numerical tsunami modelling package JAGURS (Baba et al. 2015) to simulate the tsunami
 144 propagation of the 2022 HTHH event and obtain the theoretical tsunami arrival time based on the shallow
 145 water wave speed (white contours in Figure 1). The code solves linear Boussinesq-type equations in a
 146 spherical coordinate system using a finite difference approximation with the leapfrog method. We specify

147 a unit Gaussian-shaped vertical sea surface displacement at the volcanic base as the source of
148 conventional tsunamis. For a unit source i with center at longitude φ_i and latitude θ_i , the
149 displacement distribution $Zi(\varphi, \theta)$ can be expressed as:

$$150 \quad Zi(\varphi, \theta) = \exp\left[-\frac{(\varphi-\varphi_i)^2+(\theta-\theta_i)^2}{2\sigma}\right] \quad (1)$$

151 Where we set characteristic length σ as 5 km (NASA, 2022). The bathymetric data is resampled from the
152 GEBCO 2019 with 15 arc-sec resolution (The General Bathymetric Chart of the Oceans, downloaded
153 from <https://www.gebco.net>).

154 2.3 Spectral Analysis of Tsunami Waves

155 To investigate the temporal changes of the dominant wave periods, we conduct continuous wavelet
156 transformation (frequency-time) analyses for some representative DART buoys, tide gauges and
157 barometers, in which wavelet Morlet mother function is implemented (Kristeková et al., 2006). The first
158 32-hour time series of DART buoys and barometers after the eruption (at 04:14:45 on 15 January 2022)
159 are used for source-related wavelet analysis. The first 48-hour time series of tide gauges after the eruption
160 are employed for hydrodynamics-related wavelet analysis at coastlines. We adopt the Averaged-Root-
161 Mean-Square (ARMS) method as a measure of absolute average tsunami amplitude with a moving time
162 window of 20 min to calculate the tsunami duration (Heidarzadeh and Satake, 2014). We define the time
163 durations as the time period where ARMS levels of tsunami waves are above those prior to the tsunami
164 arrivals.

165 3. Results

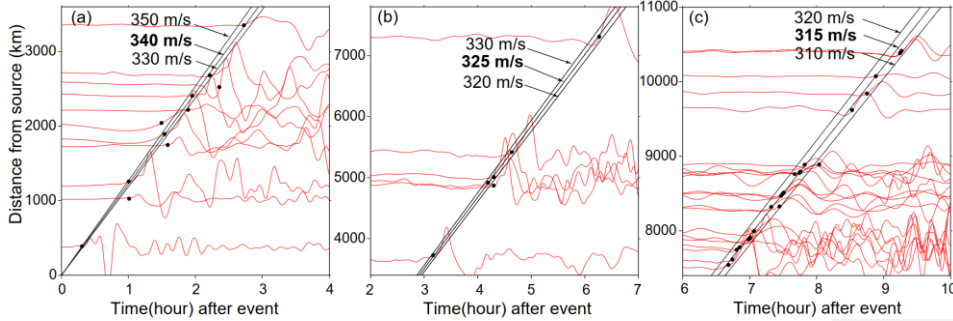
166 3.1 The decreasing propagation velocities of the Lamb Wave

167 Although many types of atmospheric waves were generated by the 2022 HTHH eruption, the most
168 prominent signature was the Lamb waves which were globally observed by ground-based and spaceborne
169 geophysical instrumentations (Kulichkov et al., 2022; Liu et al., 2022; Lin et al., 2022; Matoza et al.,
170 2022; Themens et al., 2022; Adam, 2022; Kubota et al., 2022). Interestingly, we notice that a wide range
171 of the velocities from 280 m/s to 340 m/s were proposed through observations and Lamb wave modelling
172 (e.g., Kubota et al., 2022; Lin et al., 2022; Matoza et al., 2022; Themens et al., 2022). The travelling
173 velocity of Lamb waves in real atmosphere is affected by temperature distributions, winds and dissipation

174 (Otsuka, 2022). To investigate whether the propagation speeds of the lamb wave change in space and
175 time, we analyze the waveforms recorded by the DART buoys in the Pacific Ocean. DART buoy with
176 pressure sensor deployed at the ocean's bottom records the sea level change that is transferred from
177 pressure records in Pascals, instead of direct water height. For the 2022 HTHH tsunami event, the
178 pressure fluctuation at DART buoy is a superposition of the pressure changes caused by tsunami and the
179 Lamb wave (Kubota et al., 2022). The Pacific DART buoys recorded the most discernible air-sea
180 coupling pulse in deep ocean with Lamb waves that arrived earlier than the theoretical tsunamis (Figure
181 1). The tsunami waveforms recorded by tide gauges did not clearly detect the tsunami signals associated
182 with the Lamb waves, therefore are not sufficient for further analysis (Figure 2). Thus, we estimate the
183 speed of Lamb waves using the waveforms recorded by the Pacific DART buoys. The Lamb wave
184 arrivals are limited within arrival time range from possible velocities of 280–340 m/s. The time points at
185 which the tsunami amplitudes first exceed 1 e-4 m above sea level are defined as Lamb wave arrivals.
186 By carefully fitting the arrivals with different constant velocities, we illustrate the velocities of Lamb
187 wave were generally uniform, but slightly decrease with the increase of propagation distance (Figure 3).
188 The Lamb waves initially propagated radially at speed of ~340 m/s before slowing to ~325 m/s after
189 reaching ~3400 km, and further decreasing to ~315 m/s at 7400 km. In an isothermal troposphere
190 assumption, the phase velocity of the Lamb wave (C_L) can be estimated with the following equation
191 (Gossard and Hooke, 1975b):

$$192 \quad C_L = \sqrt{\frac{\gamma R T}{M}} \quad (2)$$

193 Where $\gamma = 1.4$ (air specific heat ratio corresponding to atmospheric temperature), $R = 8314.36 \text{ J kmol}^{-1}$
194 K^{-1} (the universal gas constant), $M = 28.966 \text{ kg kmol}^{-1}$ (molecular mass for dry air) are constant for the
195 air, T is the absolute temperature in kelvin. Thus, Lamb wave velocity is mainly affected by the air
196 temperature, meaning the travelling velocity of lamb waves might decrease when propagating from
197 regions with high temperature towards those with low temperatures, e.g., the north pole. By assuming a
198 set of possible temperatures in January (Table 1), we calculated the velocities C_L could range between
199 312–343 m/s when temperatures vary between -30–20 °C. Therefore, the decreased velocity of the Lamb
200 waves could be a consequence of cooling of the air temperature.



201
202 **Figure 3. Fitting the arrival times of normalized Lamb-induced tsunami waveforms with different**
203 **velocities. Black dots mark the arrival times of the Lamb waves. Black lines represent velocities.**

204 **Table 1. Estimated Lamb wave velocities in an isothermal troposphere assumption**

Celsius temperature (°C)	thermodynamic temperature (K)	C_L (m/s)
20	293.15	343.14
10	283.15	337.23
0	273.15	331.21
-10	263.15	325.19
-20	253.15	318.86
-30	243.15	312.49

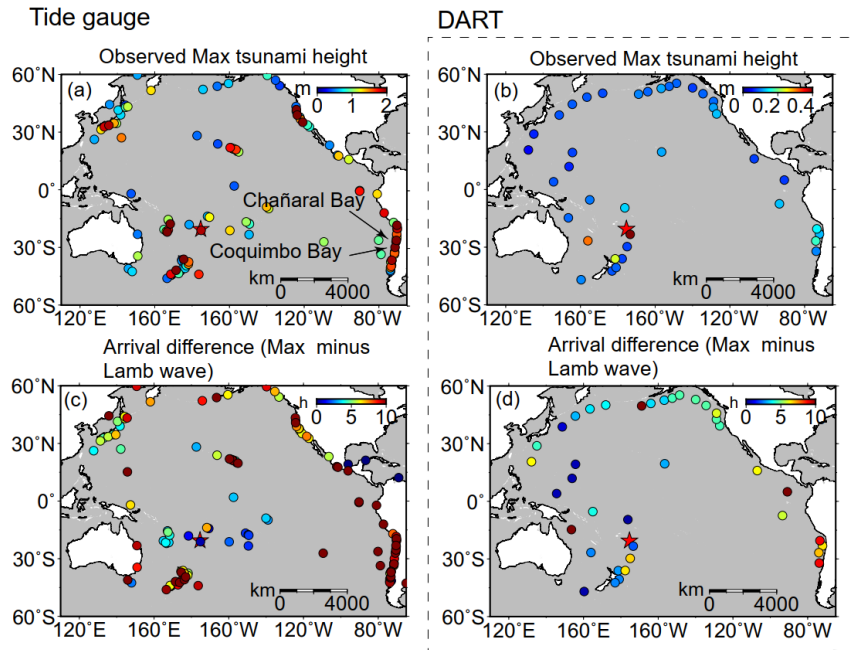
205 **3.2 Tsunami features observed by DART buoys and Tide gauges**

206 The statistics of tsunami heights and arrival times recorded at 38 DART buoys and 116 tide gauges across
207 the Pacific Ocean are used to interpret the tsunami characteristics. The comparison of the statistical
208 characters between DART and tide gauge observations yields some useful information of the
209 hydrodynamic process of tsunami propagation and help identify tsunami wave components with different
210 traveling velocities.

211 The average value of the maximum tsunami wave height (trough-to-crest) for the 116 tide gauge stations
212 is ~1.2 m. Figure 4a shows tide gauges with large tsunami heights exceeding 2 m are mainly distributed
213 in coastlines with complex geometries (Figure S1a), such as gauges at New Zealand, Japan, and north
214 and south America. For example, the largest tsunami height among tide gauges is 3.6 m at a bay-shaped
215 coastal area Chañaral in Chile (Figure S1b). In sharp contrast to tide gauges, the maximum tsunami
216 heights of most Pacific DART buoys are less than 0.2 m. The largest tsunami height in the DART buoys
217 is only ~0.4 m recorded at the nearest one, 375 km from the volcano (Figure 4b). The comparison between
218 DART buoys and tide gauges indicate that the direct contribution of air-sea coupling to the tsunami

219 heights is probably in the level of tens of centimeters (Kubota et al., 2022). The meter-scale tsunami
220 heights at the coastlines suggest the bathymetric effect could play a major role during tsunami
221 propagation. In respect to the arrival of maximum tsunami waves, the time lags between Lamb waves
222 and the maximum heights of tide gauges mainly range between ~0–10 h (Figure 4c). The delayed times
223 of ~10 h are observed in New Zealand, Hawaii, and west coast of America (Figure 4c), suggesting the
224 interaction between tsunami waves and local topography/bathymetry delays the arrival of the maximum
225 waves (e.g., Hu et al., 2022). For example, the delayed maximum tsunami height can be attributed to the
226 edge waves (Satake et al., 2020) and resonance effect (Wang et al., 2021) from tsunami interplays with
227 bays/harbors, islands, and continental shelves of various sizes. The significant regional dependence of
228 the coastal tsunami heights and the time lags of the maximum tsunami waves can be attributed to the
229 complexity of local bathymetry, such as continental shelves with different slopes, and harbor/bay with
230 different shapes and sizes (Satake et al., 2020). On the other hand, for tsunami events with earthquake
231 origins (e.g., Heidarzadeh and Satake, 2013), the first waves recorded by DART buoys are normally
232 observed as the largest wave since DART buoys are located in the deep sea and less influenced by
233 bathymetric variation. In the case of Tonga tsunami event, On the other hand, since the DART records
234 are less influenced by bathymetric variation in space, the first waves in DART buoys are supposed to be
235 the maximum tsunami waves as observed in the 2011 Tohoku tsunami event (Heidarzadeh and Satake,
236 2013). However, we observe the inconsistency between the arrivals of the Lamb wave-induced tsunami
237 waves and the maximum tsunami heights (Figure 4d). The time lags of the maximum waves of DART
238 buoys present a coarsely increasing tendency with the increasing distance from the volcano, which
239 indicates the contribution of other tsunami generation mechanism propagating with a uniform but lower
240 speed than Lamb wave.

带格式的: 默认段落字体, 字体: 10 磅, 字体颜色: 文字 1,
图案: 清除 (自定义颜色(RGB(247,247,247)))



241
 242 **Figure 4. The spatiotemporal signatures of the 2022 HTHH tsunami across the Pacific Ocean. (a)**
 243 **Observed the maximum tsunami height (trough-to-crest height) of tide gauges. (c) Arrival**
 244 **differences between the maximum tsunami height of tide gauges and Lamb waves. (b) and (d)**
 245 **are the same as (a) and (c) but for DART buoys.**

246 3.3 Tsunami components identified from wavelet analysis

247 The statistical analysis of tsunami waveforms at tide gauges and DART buoys suggest the tsunami waves
 248 likely contain several components with different source origins. To further identify these tsunami
 249 components, we conduct wavelet analysis for tsunami waveforms recorded by representative DART
 250 buoys and air pressure waveforms recorded by selected barometers. We demonstrate the analysis result
 251 through the frequency-time (f-t) plot of wavelet which shows how energy and period vary at frequency
 252 and time bands (Figure 5 and Figure 6). Tsunami components have clear signatures in all f-t plots as the
 253 energy levels are quite large when they arrive. Figure 5 shows the wavelet analysis of six DART buoys
 254 located in the vicinity of the eruption site (<3664 km). Figure 6 show the wavelet analysis of ten DART
 255 buoys located in the Pacific rim which are far away from the source location. We observe three interesting
 256 phenomena: 1) most of the tsunami wave energy is concentrated in four major period bands, i.e., 3–5
 257 min, ~10–30 min, ~30–40 min, and ~80–100 min; 2) The significant tsunami component with period

258 band of 3-5 mins are recorded by stations between the eruption site and the north tip of the New Zealand;
259 3) There exists one exceptional tsunami component with longer wave period of ~80–100 min mainly
260 recorded in the Tonga, the New Zealand and Hawaii, which travels even faster than the Lamb waves.

261 To further explore the source mechanism of these tsunami components, we take advantage of the
262 published information related to different propagating velocities of atmospheric gravity waves (Kubota
263 et al., 2022) and add four kinds of propagating velocities as criteria to differentiate the tsunami arrivals
264 from different sources (Figure 5 and Figure 6). The first reference speed is 1000 m/s related to the
265 radically propagating atmospheric shock waves near the source region (Matoza et al., 2022; Themens et
266 al., 2022). The second one is the velocities of Lamb wave ranging between 315–340 m/s derived from
267 the aforementioned analysis in section 3.1 (Figure 3). The third one is 200 m/s corresponding to the lower
268 limit of atmospheric gravity wave modes other than Lamb waves which were also excited by the volcanic
269 eruptions (Kubota et al., 2022). The last is the arrival time of conventional tsunami given by tsunami
270 modelling (Figure 1). The theoretical velocity of conventional tsunami is significantly nonuniform
271 spatially as compared with those of the atmospheric waves. The conventional tsunami propagation speed
272 is determined by the water depth along the propagation route. The velocity of non-dispersion shallow-
273 water waves (C_H) in the ocean is given by:

$$274 \quad C_H = \sqrt{g \cdot H} \quad (3)$$

275 Where g is gravity acceleration (9.81m/s^2), H is the water depth. The propagation velocities of tsunami
276 are ~296–328 m/s in the deepest trenches on earth (i.e., ~11 km in Mariana Trench and ~9 km in Tonga
277 Trench). The velocities decrease quickly to only ~44 m/s at ~200 m depth along the edge of continental
278 shelf. With the average depth of ~4–5 km, the average velocities in the Pacific Ocean range between
279 ~200–224 m/s. Thus, theoretical tsunami velocities present significant slowness and variability. We
280 delineate the arrival times of the four reference speeds in Figures 5 and 6.

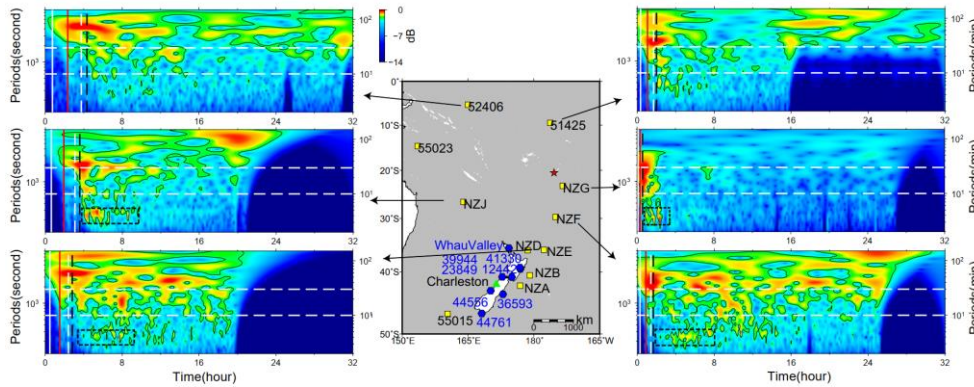
281 One particularly remarkable phenomenon is that the wave component with period of ~80–100 min
282 propagated at a very fast speed of ~1000 m/s in the vicinity of the HTHH site, i.e., New Zealand and
283 Hawaii (e.g., stations 52406, NZJ, NZE, 51425 in Figure 5, and 51407 in Fig. 6). We infer that the
284 tsunami component within ~80–100 min period band was likely produced by the atmospheric shock
285 waves during the initial stage of the volcanic eruption and spatially only cover the near-source region.
286 To verify this observation, we select 16 representative barometers located in the near-source region and

287 far-field area for wavelet analysis (see the locations in Figure 5 and Figure 6). Figure 7 shows the
288 waveforms of atmospheric pressure at selected locations and Figure 8 provides the frequency-time (f-t)
289 plot of wavelet analysis of some representative barometers. Interestingly, we are able to discern the air
290 pressure pulses prior to Lamb waves at barometers in New Zealand (the two columns on the left in Figure
291 7), although such signals are not detectable in waveforms recorded by barometers far from the source
292 (the two columns on the right in Figure 7). The spatial distribution of such unusual pressure changes
293 suggest that the fast travelling shock waves were only limited in the near-source region, as reflected in
294 the travelling ionospheric disturbances (Matoza et al., 2022; Themens et al., 2022). Additionally, we also
295 see that the long period signals of ~80–100 min appear in DART buoys far away from the eruption site.
296 Such signals may be related with the long-period gravity waves (Matoza et al., 2022).

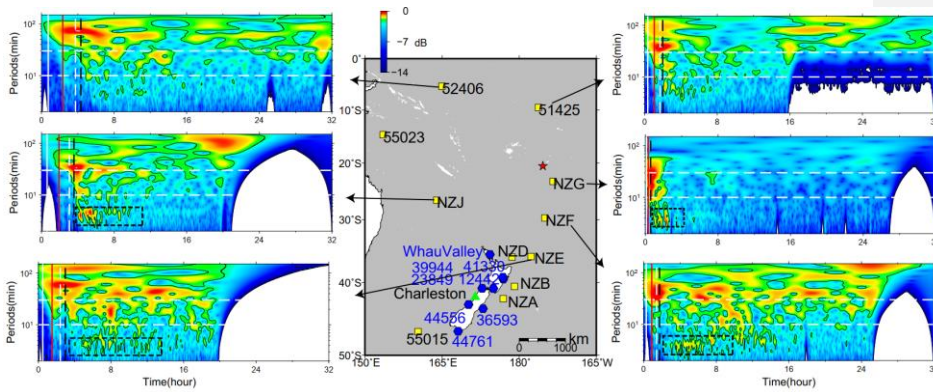
297 The tsunami components at period band of ~30–40 min can be readily associated with Lamb waves
298 because the arrival times of [the](#) tsunami waves and Lamb waves have excellent match, as shown in the
299 tsunami data recorded by DART buoys (e.g., NZJ and 51425 in Figure 5; 51407, 32401 and 32413 in
300 Figure 6) and pressure data by barometers (Figure 8).

301 For the tsunami components with the period band of ~10–30 min, although the arrivals of ~10–30 min
302 tsunami components cover some theoretical tsunami arrival times, they do not consistently match. The
303 tsunami components occurring within the time period between Lamb waves and the lower gravity waves'
304 velocities has a good agreement with the velocity range of several atmospheric gravity wave modes
305 (Matoza et al., 2022; Themens et al., 2022; Kubota et al., 2022). Similarly, the air pressure data also show
306 energy peaks at ~10–30 min period band, which is consistent with the tsunami data (Figure 8). Such
307 consistency further verifies the contribution of atmospheric gravity waves to the volcanic tsunami.

308 The tsunami components with the shortest period of ~3–5 min (stations NZE, NZF, NZG and NZJ;
309 marked with black dashed squares in Figure 5) are only observed at DART records near the eruption
310 location. Meanwhile, the arrival times of these components agree well with the modelled arrivals of
311 conventional tsunamis. Thus, we believe the observed shortest period band should originate from the
312 seafloor crustal deformation. We further infer that this component could be generated by the partial
313 underwater caldera collapse and/or subaerial/submarine landslide failures associated with 2022 HTHH
314 volcanic eruption.

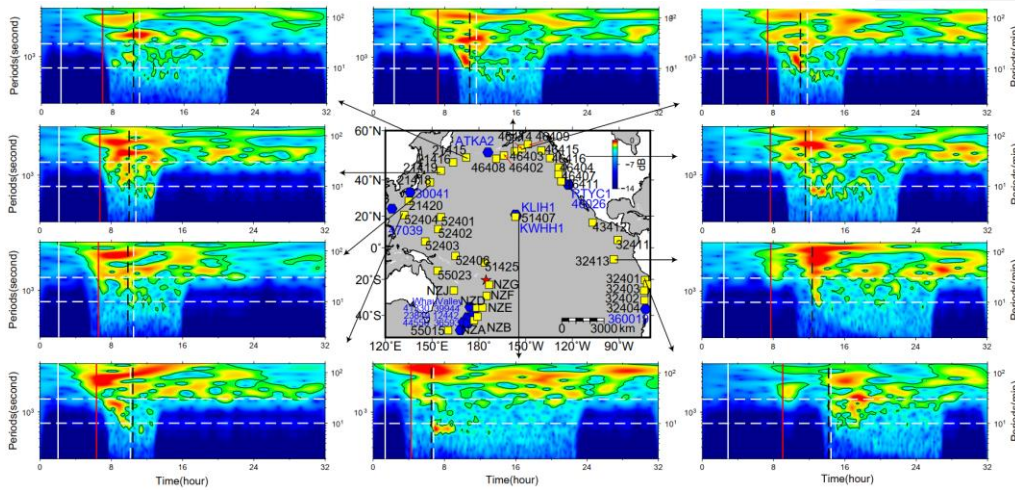


315

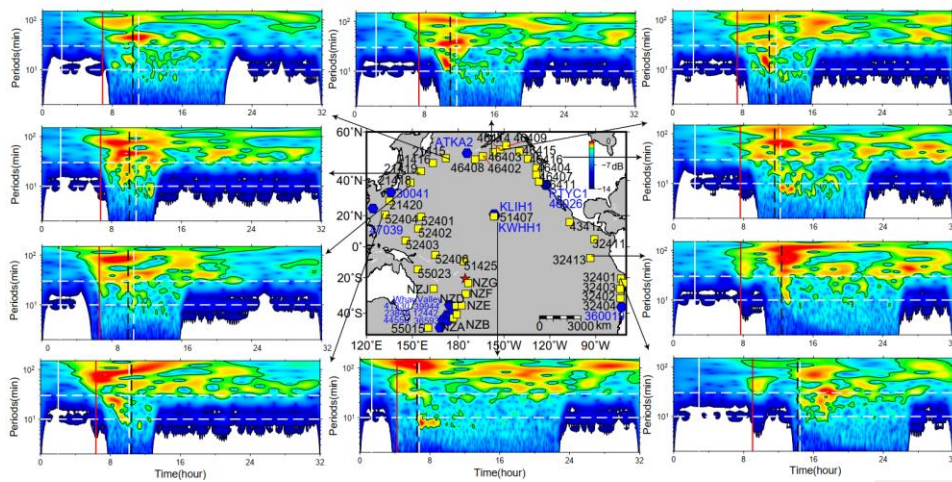


316

317 **Figure 5. Wavelet analysis of representative DART buoys in the vicinity of the HTHH volcano. In**
 318 **each sub-plot, the solid vertical white lines mark the arrival time with travelling velocity of 1000**
 319 **m/s. The solid vertical red lines mark the arrivals of Lamb waves. The dashed vertical white lines**
 320 **mark lower limit of AGWs' velocity of 200 m/s (Kubota et al., 2022). The dashed vertical black**
 321 **lines represent the theoretical tsunami arrivals. The dashed horizontal white lines mark two**
 322 **reference wave periods of 10 min and 30 min. The blue hexagons represent the locations of**
 323 **barometers. Green triangle makes the location of the tide gauges at Charleston. Decibel (dB) is**
 324 **calculated from: $dB = 10 \log(A/A_0)$, where A is wavelet power, A_0 is a reference wavelet power of**
 325 **the maximum one (Thomson and Emery, 2014).**

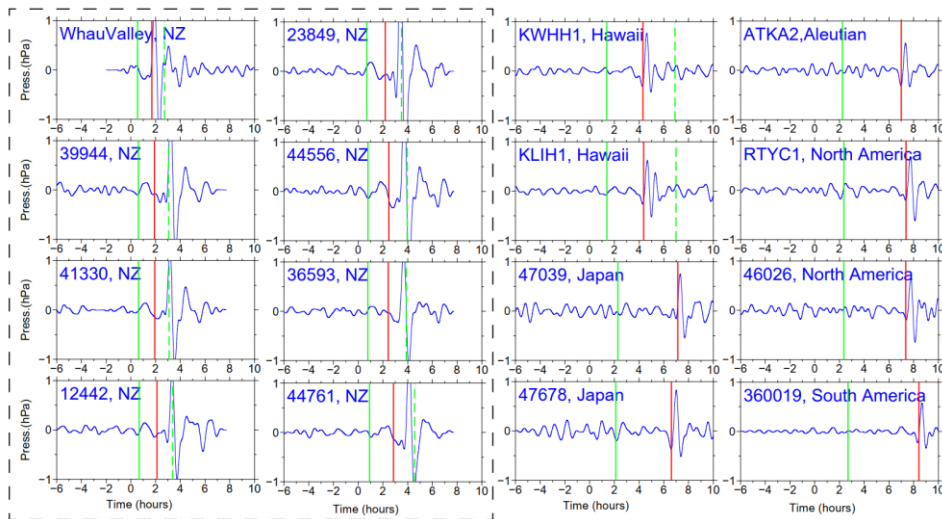


326



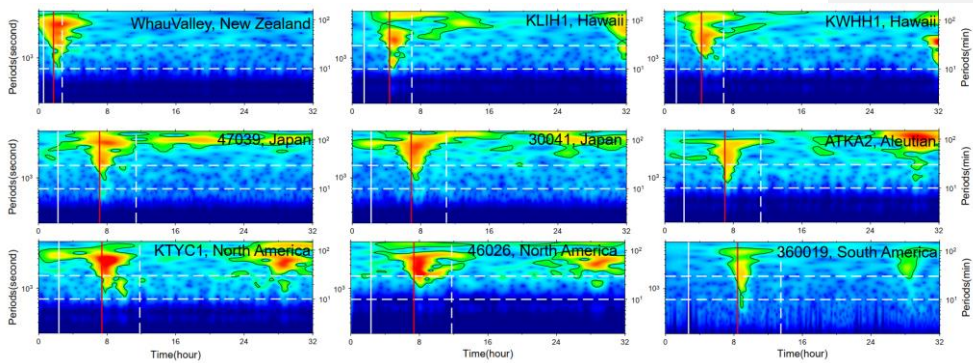
327

328 **Figure 6. Wavelet analysis of representative DART buoys far away from the HTHH volcano. In**
 329 **each sub-plot, the solid vertical white lines mark the arrival time with travelling velocity of 1000**
 330 **m/s. The solid vertical red lines mark the arrivals of Lamb waves. The dashed vertical white lines**
 331 **mark lower limit of AGWs' velocity of 200 m/s. The dashed vertical black lines represent the**
 332 **theoretical tsunami arrivals. The dashed horizontal white lines mark two reference wave periods**
 333 **of 10 min and 30 min. The blue hexagons represent the locations of barometers.**

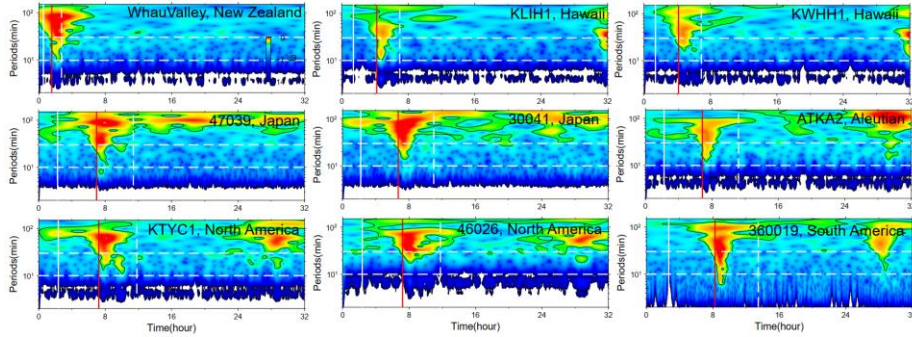


334

335 **Figure 7. Shockwave-related atmospheric pressure waveforms of selected barometers in the Pacific**
 336 **Ocean. All traces have been filtered between 30 min and 150 min. In each sub-plot, the solid vertical**
 337 **green lines mark the arrival time with travelling velocity of 1000 m/s. The solid vertical red lines**
 338 **mark the arrivals of Lamb waves. The dashed vertical green lines mark lower limit of AGWs'**
 339 **velocity of 200 m/s.**



340



341
 342 **Figure 8. Wavelet analysis of some representative barometers. In each sub-plot, the solid vertical**
 343 **white lines mark the arrival time with travelling velocity of 1000 m/s. The solid vertical red lines**
 344 **mark the arrivals of Lamb waves. The dashed vertical white lines mark lower limit of AGWs’**
 345 **velocity 200 m/s. The dashed horizontal white lines mark three reference periods of 10 min and 60**
 346 **min.**

347 **4. Discussion**

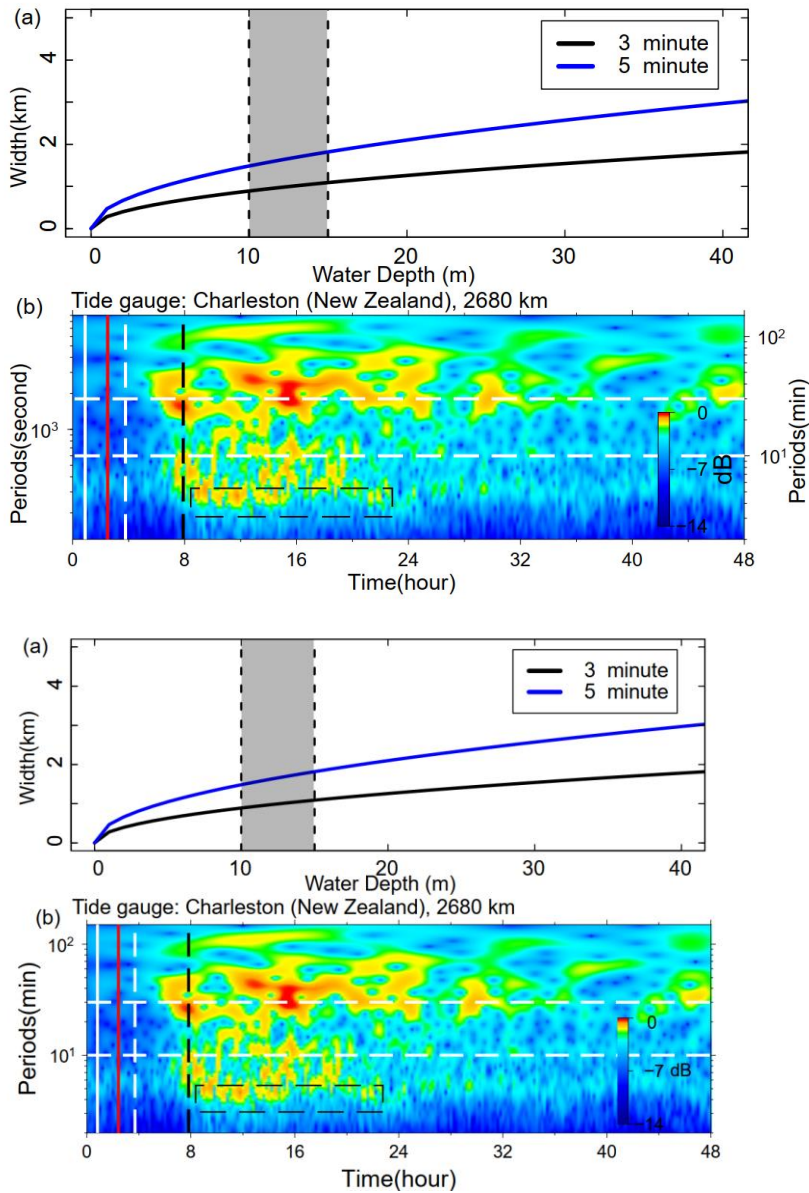
348 **4.1 Tsunami from Caldera Collapse and Its Long-distance Traveling Capability**

349 The tsunami wave energy distributed in different period bands is identified with reference arrival times.
 350 The tsunami component with 3–5 min period is most likely generated by seafloor crustal deformation in
 351 the volcanic site, but specific mechanism is not determined. A variety of possible scenarios associated
 352 with the eruption could be responsible for the near-field tsunami waves, such as volcanic earthquakes,
 353 pyroclastic flows entering the sea, underwater caldera flank collapse, and subaerial/submarine failures
 354 (Self and Rampino, 1981; Pelinovsky et al., 2005). To further investigate the source mechanism, we
 355 apply a simplified model (Rabinovich, 1997) to estimate the probable dimension of tsunami source:

356
$$L = \frac{T\sqrt{gH}}{2} \quad (4)$$

357 Where L is the typical dimension (length or width) of the tsunami source, H is average water depth in the
 358 source area, g is the gravity acceleration, and T is primary tsunami period. By comparing with the post-
 359 2015 morphology of the HTHH caldera which was obtained through drone photogrammetry and
 360 multibeam sounder surveys, Stern et al. (2022) estimate that much of the newly-formed Hunga Tonga
 361 Island and the 2014/2015 cone were destroyed by the 2022 eruption, and the vertical deformation of
 362 Hunga Ha’apai Island is ~10–15 m (Stern et al., 2022). With no more quantitative constraint of the
 363 seafloor deformation, we tentatively assume H as 10–15 m, then the possible dimension of seafloor

364 crustal deformation responsible for the small-scale tsunami could be in the scale of 0.8–1.8 km (Figure
 365 9a). The estimated size is very likely from partial caldera collapse that usually has limited scale in
 366 volcanic site (Ramalho et al., 2015; Omira et al., 2022). If it is the case, the partial flank collapse could
 367 be located between Hunga Tonga and Hunga Ha'apai Islands.



370 **Figure 9. Mechanism of tsunami component with 3–5min period. (a) The source dimension**
371 **estimated by equation 4. (b) Wavelet analysis of tide gauge at Charleston, New Zealand, 2680 km**
372 **away from the eruption site. The solid vertical white line marks the arrival time with travelling**
373 **velocity of 1000 m/s. The solid vertical red line marks the arrival of Lamb wave. The dashed**
374 **vertical white line marks lower limit of AGWs' velocity 200 m/s. The dashed vertical black line**
375 **marks the theoretical tsunami arrivals.**

376 An interesting phenomenon is that the tsunami component with 3–5 min period can still be observed in
377 a bay-shaped coastal area at Charleston in New Zealand (see the location in Figure 5) which is 2680 km
378 away from the eruption site and maintains a high energy level lasting up to 14 h (Figure 9b). The long-
379 traveling capability could be associated with the ~ 10000 m deep water depth of the Tonga Trench that
380 keeps the source signals from substantial attenuation. In deep open ocean, the wavelength of a tsunami
381 can reach two hundred kilometers, but the height of the tsunami may be only a few centimeters. Tsunami
382 waves in the deep ocean can travel thousands of kilometers at high speeds, meanwhile losing very little
383 energy in the process. The long oscillation can be attributed to the multiple reflections of the incoming
384 waves trapped in the shallow-water bay at Charleston.

385 Generally, devastating tsunamis with long-distance travelling capability are mostly generated by
386 megathrust earthquakes (Titov et al., 2005). Caldera collapses or submarine landslides with limited scale
387 normally only generate local tsunamis, e.g., the 1998 PNG (Papua New Guinea) tsunami event (Kawata
388 et al., 1999) and the 1930 Cabo Girão tsunami event (Ramalho et al., 2015). Therefore, it's exceptional
389 that the tsunami component from scale-limited failure could travel at-least 2680 km away from the
390 eruption site. It demonstrates that tsunamis from small-scale tsunamigenic source have the capability to
391 travel long distance and cause long oscillation at favored condition, e.g., deep trench, ocean ridge and
392 bay-shaped coasts.

393 **4.2 The Possible Mechanisms of Long Tsunami Oscillation**

394 An important tsunami behavior of the 2022 HTHH tsunami is the long-lasting oscillation ~ 3 days in the
395 Pacific Ocean (Figure 10a), which is comparable to that of the 2011 Tohoku tsunami, ~4 days
396 (Heidarzadeh and Satake, 2013). We demonstrate the duration time of the tsunami oscillation through
397 ARMS (Averaged-Root-Mean-Square) approach that is a measure of absolute average tsunami amplitude
398 in a time period. The long-lasting tsunami energy can be observed at many regions, such as the coasts of
399 New Zealand, Japan, Aleutian, Chile, Hawaii, and west coasts of America. Several mechanisms could

400 account for the long-lasting tsunami, including (1) Lamb waves circling the Earth multiple times
401 (Amores et al., 2022; Matoza et al., 2022), (2) resonance effect between ocean waves and atmospheric
402 waves (Kubota et al., 2022), and (3) bathymetric effect. We discuss the contribution of each mechanism
403 in the following section.

404 To investigate the contribution of Lamb wave to the long-lasting tsunami, we compare the air pressure
405 disturbances recorded by selected barometers together with the tsunami waveforms of nearby tide gauges
406 (Figure 10b). While the barometers present discernible wave pulses at each Lamb wave's arrival, only
407 the first Lamb wave triggered clear tsunami signal and no detectable tsunami signatures correspond to
408 the following passage, suggesting the Lamb waves do not directly contribute to the long oscillation.

409 ~~Theoretically, the resonance effects between ocean waves and atmospheric waves could contribute to~~
410 ~~the long oscillation on coastlines based on the following reasons. Besides the Lamb wave, Watanabe et~~
411 ~~al., 2022, detected internal Pekeris wave which propagate with a slower horizontal phase speed of ~245~~
412 ~~m/s and gravity waves with even slower propagation speed by analyzing radiance observations taken~~
413 ~~from the Himawari-8 geostationary satellite. Atmospheric waves with such speeds are more likely to~~
414 ~~resonant with the conventional tsunami waves and provide continuous energy supply (Kubota et al.,~~
415 ~~2022). First, part of the atmospheric gravity waves propagated at velocities close to averaged velocities~~
416 ~~of conventional tsunami in the Pacific Ocean (198–221 m/s) which resulted in the resonance with ocean~~
417 ~~waves (Kubota et al., 2022). Second, when Lamb wave speed approaches the tsunami speed, Proudman~~
418 ~~resonance gradually increase tsunami heights, wherein Proudman resonance optimally maximizes~~
419 ~~tsunami heights when they match well. In deep oceanic trenches, such as Mariana and Tonga-Kermadec~~
420 ~~trench (10000–11000 m), tsunami velocities range between 314–330 m/s which are comparable with~~
421 ~~those of the observed Lamb waves 315–340 m/s. Therefore, the resonance effect could be a possible~~
422 ~~source of increased wave energy, especially in the deep trenches (Lynett et al., 2022; Tanioka et al., 2022).~~

423 To examine the role of local bathymetry in the long-lasting tsunami, we choose a well-studied and well-
424 recorded event: the 2011 Mw 9.0 Tohoku tsunami as a reference event and compare the tsunami records
425 of these two events at the same coastal stations. Although the two tsunami events were generated by
426 completely different mechanisms, i.e., large-scale seafloor deformation for the Mw 9.0 megathrust
427 earthquake (Mori et al., 2011) and fast-moving atmospheric waves for the Mw 5.8 volcanic eruption
428 (Matoza et al., 2022), they both produced widespread transoceanic tsunamis which were well recorded

带格式的: 默认段落字体, 字体: 10 磅, 字体颜色: 文字 1,
图案: 清除 (自定义颜色(RGB(247,247,247))), 非突出显示

域代码已更改

带格式的: 默认段落字体, 字体: 10 磅, 字体颜色: 文字 1,
图案: 清除 (自定义颜色(RGB(247,247,247))), 非突出显示

429 in the Pacific DART buoys and tide gauges. In the near-field, the 2011 Tohoku earthquake produced
430 runup up to 40 m at Miyako in the Iwate Prefecture in Japan's Tohoku region, ~70 km from the source
431 (Mori et al., 2011), (Mori et al., 2011). The epicenter is approximately 70 km east coast of the Oshika
432 Peninsula of Tohoku region. while However, the 2022 HTHH tsunami produced only ~13 m runup in the
433 near field from eyewitness accounts in Kanokupolu, 60 km from the volcano (Lynett et al., 2022).
434 However, in the far-field (>1000 km), we observe comparable tsunami wave heights in certain coastal
435 regions. Based on the tsunami records at 21 tide gauges surrounding the Pacific Ocean, Heidarzadeh &
436 Satake (2013) calculated the average value of the maximum tsunami heights (trough-to-crest) of the 2011
437 Tohoku tsunami is 1.6 m with the largest height of 3.9 m at the Coquimbo Bay in Chile (Heidarzadeh
438 and Satake, 2013). Coincidentally, the statistics of 116 tide gauges in this study also suggest the average
439 tsunami heights of the 2022 HTHH tsunami is around the same order, ~1.2 m, among which, the largest
440 height is 3.6 m at Chañaral Bay in Chile. Interestingly, in the coastal region of South America, the
441 locations of the largest tsunami heights of both events are adjacent (Figure 4a), i.e., Coquimbo (the 2011
442 Tohoku) and Chañaral (The 2022 HTHH).
443 To further compare the far-field hydrodynamic processes between these two events quantitatively, we
444 conduct wavelet analysis for four representative tide gauges distributed across the Pacific Ocean, i.e.
445 coastal gauges at East Cape in New Zealand, Kwajalein Island, Wake Island, and Talcahuaho in Chile
446 (see their locations in Figures 10b). The temporal changes of tsunami energy of both events can be seen
447 in Figure 11. At each tide gauge, the tsunami energy of the 2011 HTHH (Figure 11a) and the 2022 Tohoku
448 tsunamis (Figure 11b) for the first few hours after the arrivals is nonuniform with different significant
449 peaks distributed within a wide period band of ~3–100 min. Then, the following long-lasting energy of
450 the both at each station presents similar pattern and is concentrated at identical and fairly narrower period
451 channel, i.e., ~20–30 min at East Cape in New Zealand, ~40–60 min at Kwajalein Island, ~10 min at
452 Wake Island, and ~100 min at Talcahuaho in Chile, which reflects the local bathymetric effects of natural
453 permanent oscillations (Hu et al., 2022; Satake et al., 2020). Specifically, many bathymetric effects can
454 contribute to the long-lasting tsunami, such as multiple reflections across the basins, or the continental
455 shelves, and the excited tsunami resonance in bays/harbors with variable shapes and sizes (Aranguiz et
456 al., 2019; Satake et al., 2020). For example, tide gauges around New Zealand are primarily distributed in
457 harbors/ports with major natural oscillation modes of ~20–30 min (De Lange and Healy, 1986; Lynett et

带格式的: 字体: (中文) + 中文正文 (等线), 图案: 清除 (自定义颜色(RGB(247,247,247)))

带格式的: 默认段落字体, 字体: 10 磅, 字体颜色: 文字 1, 图案: 清除 (自定义颜色(RGB(247,247,247)))

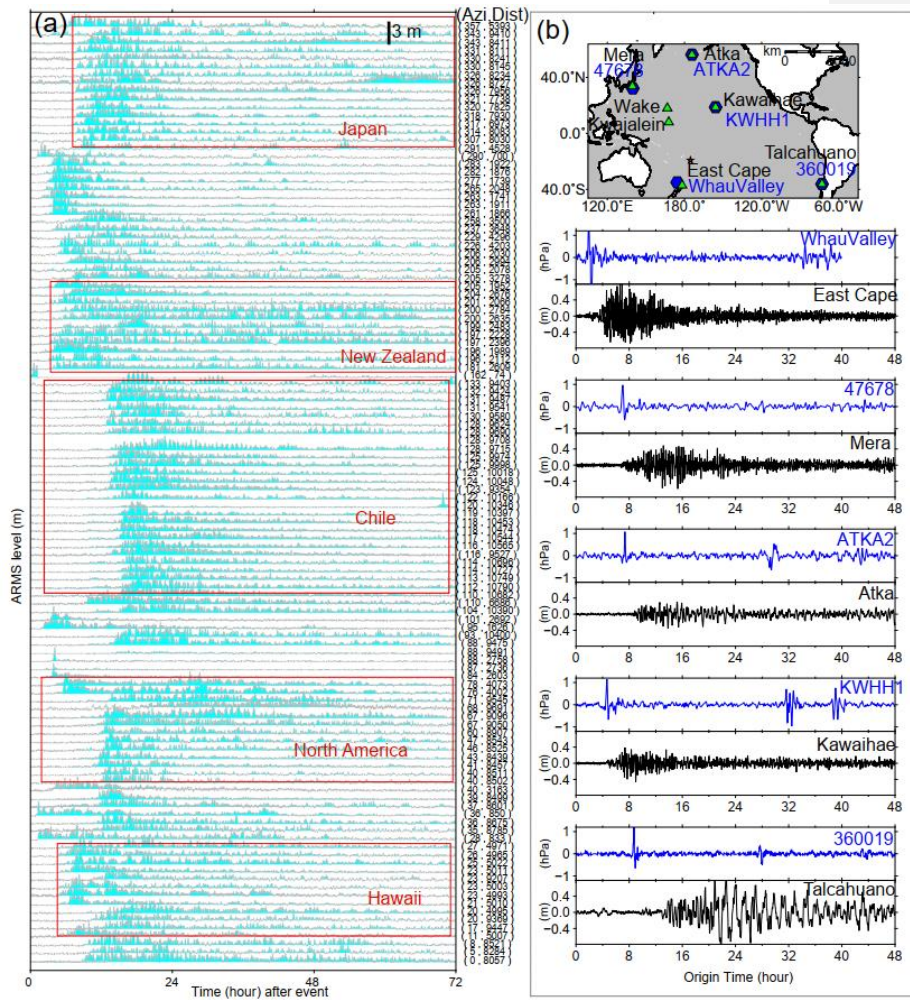
带格式的: 检查拼写和语法

域代码已更改

域代码已更改

带格式的: 默认段落字体, 字体: 10 磅, 字体颜色: 文字 1, 图案: 清除 (自定义颜色(RGB(247,247,247)))

458 al., 2022). The first oscillation mode of central Chile is centered around ~100 min (Aranguiz et al., 2019).
459 Consequently, Figure 11 illustrates that the long-lasting tsunami energy of the two events is respectively
460 distributed in 20–30 min period at East Cape in New Zealand and in ~100 min period at Talcahuaho in
461 central Chile. The coupling of bathymetric oscillation mode with tsunami containing similar-period wave
462 results in the excitement of tsunami resonance, which amplifies tsunami waves and prolongs the tsunami
463 oscillation at the two stations (Heidarzadeh et al., 2019, 2021; Hu et al., 2022; Wang et al., 2022).
464 Simply put, we do not have clear evidence that atmospheric acoustic-gravity waves from the 2022 HTHH
465 eruption directly contribute to the long-lasting tsunami, but the resonance effect associated with ocean
466 waves could a possible source of increased wave energy and amplification. However, the similarity of
467 far-field hydrodynamic behaviors between the 2022 HTHH volcanic tsunami and the 2011 Tohoku
468 seismogenic tsunami well demonstrates the both went through similar hydrodynamic processes after their
469 arrivals. The consistency favors that the long-lasting tsunami of 2022 HTHH tsunami event can very
470 likely be attributed by the interplays between local bathymetry and conventional tsunami left after each
471 passage of atmospheric waves, which can well explain why the two completely distinct tsunami events
472 possess a comparable duration time.

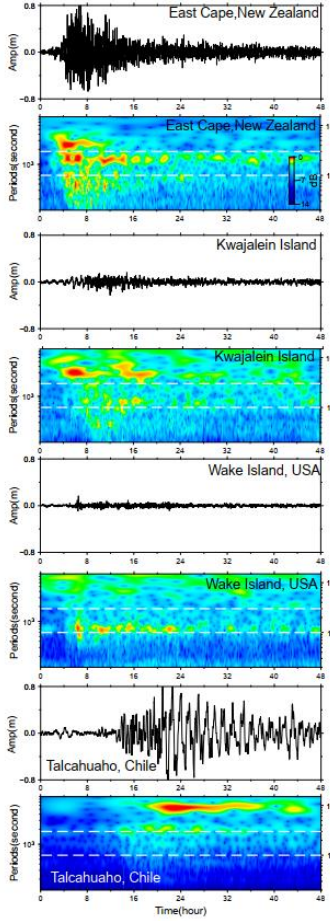


473

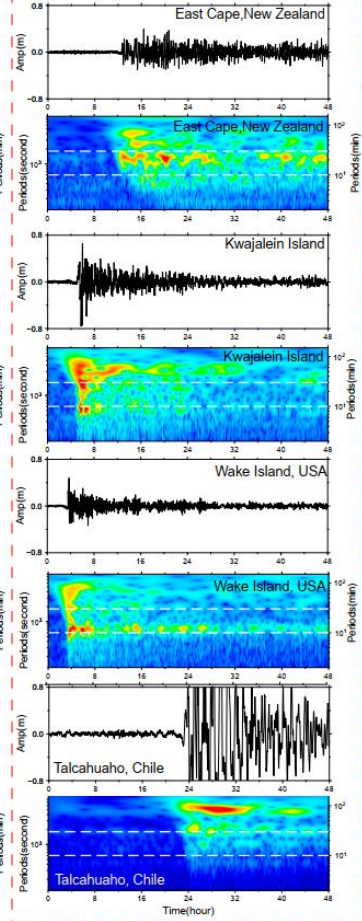
474 **Figure 10. Tsunami duration. (a) Tsunami durations at Pacific 116 tide gauges through ARMS level**
 475 **approach. (b) the location of barographs (blue curves) and nearby tide gauges (green curves), as**
 476 **well as their waveforms.**

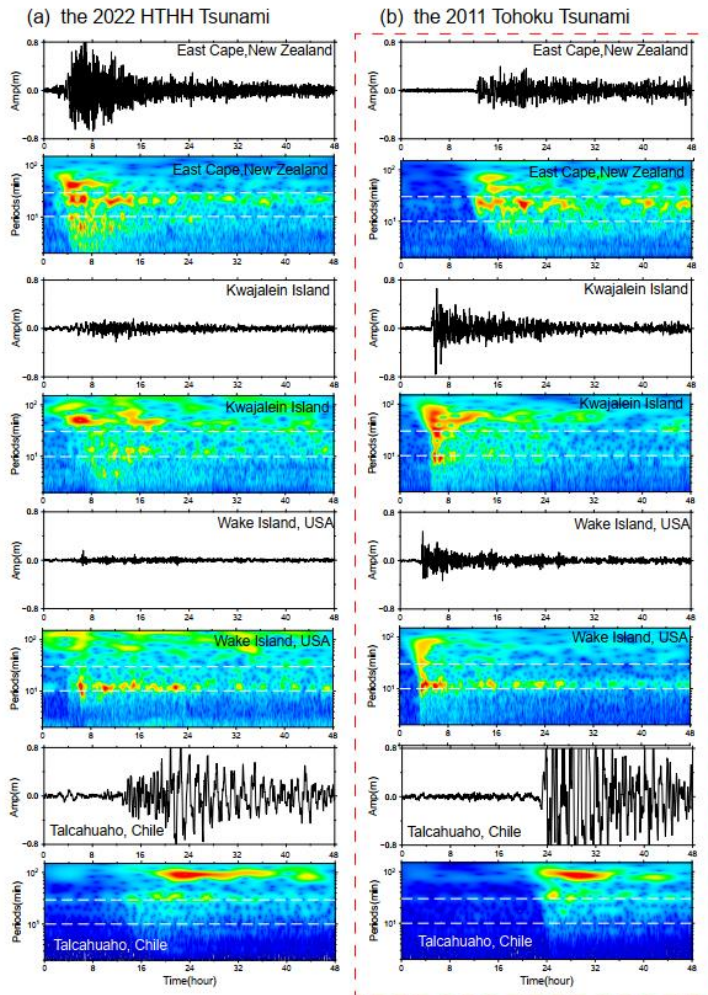
477

(a) the 2022 HTHH Tsunami



(b) the 2011 Tohoku Tsunami





479
 480 **Figure 11. Wavelet analysis of tsunami waveforms recorded by 4 tide gauges during (a) the 2022**
 481 **HTHH tsunami event, and (b) the 2011 Tohoku tsunami event. Horizontal white dashed lines**
 482 **respectively mark reference periods of 10 min and 30 min.**

483 **4.3 Challenges for Tsunami Warning**

484 The generation mechanisms and hydrodynamic characteristics of the 2022 HTHH volcanic tsunami are
 485 more complicated than pure seismogenic tsunami, which challenge the traditional tsunami warning
 486 approach.

487 The first challenge is posed by the tsunami components with propagating velocities faster than the

488 conventional tsunami. The Tonga volcanic tsunami event provides an excellent example which highlights
489 that the tsunamigenic mechanisms are not limited to tectonic activities related with the sudden seafloor
490 displacements, but also include a variety of atmospheric waves with distinct propagation velocities. The
491 tsunami components in 2022 HTHH event generated by the air-sea coupling possess a wide range of
492 velocities from 1000 m/s to 200 m/s. The Lamb waves recorded in both the 2022 HTHH event and the
493 1833 Krakatoa volcanic event traveled along the Earth's surface globally for several times (Carvajal et
494 al., 2022). The tsunami waves produced by Lamb waves, the wave components associated with resonance
495 of the air-sea coupling and their superimposition increase the difficulty of tsunami warning.
496 Another critical challenge is associated with the interplays between tsunami waves and local bathymetry.
497 The tsunami waves left by each passage of the atmospheric waves can interact with local bathymetry at
498 coastlines, such as continental shelves with different slopes, and harbor/bay with different shapes and
499 sizes. The interaction can intensify the tsunami impact and excite a variety of natural oscillation periods.
500 The 2022 HTHH tsunami with an extremely wide period range of ~2–100 min have a great potential to
501 couple with the excited natural oscillations and form extensive tsunami resonance phenomena. The
502 resonance effects result in long-lasting oscillation and delayed tsunami wave peaks. The uncertain
503 arrivals of the maximum tsunami waves pose an extra challenge to tsunami warning.

5045. **Conclusion**

505 In the study, we explore the tsunamigenic mechanisms and the hydrodynamic characteristics of the 2022
506 HTHH volcanic tsunami event. Through extensive analysis of waveforms recorded by the DART buoys,
507 tide gauges and barometers in the Pacific Ocean, we reach the main findings as follows:

508 (1) We identify four distinct tsunami wave components based on their distinct propagation velocities or
509 period bands (~80–100 min, 10–30 min, 30–40 min, and 3–5 min). The generation mechanisms of these
510 tsunami components range from air-sea coupling to seafloor crustal deformation during the volcanic
511 eruption.

512 (2) The first-arriving tsunami component with 80–100 min period was most likely from shock wave
513 spreading at a velocity of ~1000 m/s in the vicinity of the eruption. This tsunami component was not
514 clearly identified by currently available publication and it's not easy to be visually observed through time
515 series of the waveforms. The physical mechanism is yet to be understood. The second tsunami component

516 with 30–40 min period was from Lamb waves, and was the most discussed tsunami source of this event
517 so far. A thorough analysis of DART measurements indicates that the Lamb waves traveled at the speed
518 of ~340 m/s in the vicinity of the eruption and decreased to ~315 m/s when traveling away due to cooling
519 of the air temperature. The third tsunami component was from some atmospheric gravity wave modes
520 with propagation velocity faster than 200 m/s but slower than Lamb waves. The last tsunami component
521 with the shortest periods 3-5 min was probably produced by partial caldera collapse with estimated
522 dimension of ~0.8–1.8 km.

523 (3) Although the resonance effect with the atmospheric acoustic-gravity waves ~~theoretically~~ could be a
524 source of increased wave energy, its direct contribution to the long-lasting oscillation is not demonstrated
525 yet. However, the comparison of hydrodynamical characteristics between the 2022 HTHH tsunami event
526 and the 2011 Tohoku tsunami event well demonstrated that the interactions between the ocean waves left
527 by atmospheric waves and local bathymetry contribute to the long-lasting Pacific oscillation of the 2022
528 tsunami event.

529 (4) The extraordinary features of this rare volcanic tsunami event challenge the current tsunami warning
530 system which is mainly designed for seismogenic tsunamis. It is necessary to improve the awareness of
531 people at risks about the potential tsunami hazards associated with volcanic eruptions. New approaches
532 are expected to be developed for tsunami hazard assessments with these unusual sources: various
533 atmospheric waves radiated by volcanic eruptions besides those traditionally recognized, e.g.
534 earthquakes, landslides, caldera collapses and pyroclastic flows etc.

535 **Acknowledgment**

536 This work was supported by National Natural Science Foundation (No 41976197, No 12002099),
537 Innovation Group Project of Southern Marine Science and Engineering Guangdong Laboratory (Zhuhai)
538 (No. 311021002), Key Research and Development Program of Hainan Province (No. ZDYF2020209),
539 Southern Marine Science and Engineering Guangdong Laboratory (Zhuhai) (SML2021SP305) and
540 Fundamental Research Funds for the Central Universities, Sun Yat-sen University (2021qntd23).

541 The JAGURS tsunami simulation code is employed for tsunami modelling (Baba et al., 2015;
542 <https://zenodo.org/record/6118212#.Yk98qdtBxPY>). Bathymetry data are obtained from GEBCO at
543 <http://www.gebco.net>. The sea level records in deep ocean are available from the Deep Ocean Assessment

544 and Reporting of Tsunamis (DART) buoy network in the Pacific (<https://nctr.pmel.noaa.gov/Dart/>), and
545 GeoNet New Zealand DART network (<https://tilde.geonet.org.nz>). The sea level records of tide gauges
546 are downloaded from UNESCO/ IOC (<http://www.ioc-sealevelmonitoring.org/>). Barometer data are
547 provided by the following providers: Direcció'n Meteoroló'gica de Chile
548 (<https://climatologia.meteochile.gob.cl>), NOAA National Weather Service
549 (<https://www.weather.gov/ilm/observations>), Japan Meteorological Agency (<https://www.jma.go.jp>),
550 The UK Met Office Weather Observation (<https://www.metoffice.gov.uk/observations>), and Fiji
551 Meteorological Service (<https://www.met.gov.fj>).

552 **Reference**

553 Adam, D.: Tonga volcano created puzzling atmospheric ripples, *Nature*,
554 <https://doi.org/10.1038/d41586-022-00127-1>, 2022.

555 Amores, A., Monserrat, S., Marcos, M., Argüeso, D., Villalonga, J., Jordà, G., and Gomis, D.:
556 Numerical simulation of atmospheric Lamb waves generated by the 2022 Hunga-Tonga volcanic
557 eruption, *Geophys. Res. Lett.*, 49, e2022GL098240, <https://doi.org/10.1029/2022GL098240>, 2022.

558 Aranguiz, R., Catalán, P. A., Cecioni, C., Bellotti, G., Henriquez, P., and González, J.: Tsunami
559 Resonance and Spatial Pattern of Natural Oscillation Modes With Multiple Resonators, *J. Geophys.*
560 *Res. Ocean.*, 124, 7797–7816, <https://doi.org/10.1029/2019JC015206>, 2019.

561 Baba, T., Takahashi, N., Kaneda, Y., Ando, K., Matsuoka, D., and Kato, T.: Parallel Implementation of
562 Dispersive Tsunami Wave Modeling with a Nesting Algorithm for the 2011 Tohoku Tsunami, *Pure*
563 *Appl. Geophys.*, 172, 3455–3472, <https://doi.org/10.1007/s00024-015-1049-2>, 2015.

564 Bevis, M., Taylor, F. W., Schutz, B. E., Recy, J., Isacks, B. L., Helu, S., Singh, R., Kendrick, E.,
565 Stowell, J., Taylor, B., and Calmantli, S.: Geodetic observations of very rapid convergence and back-
566 arc extension at the tonga arc, *Nature*, 374, 249–251, <https://doi.org/10.1038/374249a0>, 1995.

567 Billen, M. I., Gurnis, M., and Simons, M.: Multiscale dynamics of the Tonga–Kermadec subduction
568 zone, *Geophys. J. Int.*, 153, 359–388, <https://doi.org/10.1046/j.1365-246X.2003.01915.x>, 2003, 2003.

569 Carvajal, M., Sepúlveda, I., Gubler, A., and Garreaud, R.: Worldwide Signature of the 2022 Tonga
570 Volcanic Tsunami, *Geophys. Res. Lett.*, 49, e2022GL098153, <https://doi.org/10.1029/2022GL098153>,
571 2022.

572 Duncombe, J.: The Surprising Reach of Tonga's Giant Atmospheric Waves.pdf, *Eos* (Washington.
573 DC), 103, <https://doi.org/10.1029/2022EO220050>, 2022.

574 Edmonds, M.: Hunga-Tonga-Hunga-Ha'apai in the south Pacific erupts violently, *Temblor*,
575 <https://doi.org/10.32858/temblor.231>, 2022.

576 Garvin, J. B., Slayback, D. A., Ferrini, V., Frawley, J., Giguere, C., Asrar, G. R., and Andersen, K.:
577 Monitoring and Modeling the Rapid Evolution of Earth's Newest Volcanic Island: Hunga Tonga
578 Hunga Ha'apai (Tonga) Using High Spatial Resolution Satellite Observations, *Geophys. Res. Lett.*, 45,
579 3445–3452, <https://doi.org/10.1002/2017GL076621>, 2018.

580 Gossard, E. E. and Hooke, W. H.: *Waves in the Atmosphere: Atmospheric Infrasound and Gravity*
581 *Waves—Their Generation and Propagation*, Elsevier, 1975a.

582 Gossard, E. E. and Hooke, W. H.: *Waves in the Atmosphere*, Amsterdam: Elsevier, 1975b.

583 Heidarzadeh, M. and Satake, K.: Waveform and Spectral Analyses of the 2011 Japan Tsunami Records
584 on Tide Gauge and DART Stations Across the Pacific Ocean, *Pure Appl. Geophys.*, 170, 1275–1293,
585 <https://doi.org/10.1007/s00024-012-0558-5>, 2013.

586 Heidarzadeh, M. and Satake, K.: Excitation of Basin-Wide Modes of the Pacific Ocean Following the
587 March 2011 Tohoku Tsunami, *Pure Appl. Geophys.*, 171, 3405–3419, [https://doi.org/10.1007/s00024-](https://doi.org/10.1007/s00024-013-0731-5)
588 013-0731-5, 2014.

589 Hu, G., Feng, W., Wang, Y., Li, L., He, X., Karakaş, Ç., and Tian, Y.: Source characteristics and
590 exacerbated tsunami hazard of the 2020 Mw 6.9 Samos earthquake in eastern Aegean Sea, *J. Geophys.*
591 *Res. Solid Earth*, 127, e2022JB023961, <https://doi.org/10.1029/2022JB023961>, 2022.

592 Kawata, Y., Benson, B. C., Borrero, J. C., Borrero, J. L., Davies, H. L., Lange, W. P. de, Imamura, F.,
593 Letz, H., Nott, J., and Synolakis, C. E.: Tsunami in Papua New Guinea Was as Intense as First
594 Thought, *Eos, Trans. Am. Geophys. Union*, 80, 9, <https://doi.org/10.1029/99EO00065>, 1999.

595 Kristeková, M., Kristek, J., Moczo, P., and Day, S. M.: Misfit Criteria for Quantitative Comparison of
596 Seismograms, *Bull. Seismol. Soc. Am.*, 96, 1836–1850, <https://doi.org/10.1785/0120060012>, 2006.

597 Kubota, T., Saito, T., and Nishida, K.: Global fast-traveling tsunamis by atmospheric pressure waves
598 on the 2022 Tonga eruption, *Science* (80-.), <https://doi.org/10.1126/science.abo4364>, 2022.

599 Kulichkov, S. N., Chunchuzov, I. P., Popov, O. E., Gorchakov, G. I., Mishenin, A. A., Perepelkin, V.
600 G., Bush, G. A., Skorokhod, A. I., Yu. A. Vinogradov, Semutnikova, E. G., Šepic, J., Medvedev, I. P.,

601 Gushchin, R. A., Kopeikin, V. M., Belikov, I. B., Gubanova, D. P., and A. V. Karpov & A. V.
602 Tikhonov: Acoustic-Gravity Lamb Waves from the Eruption of the Hunga-Tonga-Hunga-Hapai
603 Volcano, Its Energy Release and Impact on Aerosol Concentrations and Tsunami, *Pure Appl.*
604 *Geophys.*, <https://doi.org/10.1007/s00024-022-03046-4>, 2022.
605 Lamb, H.: *Hydrodynamics*, Cambridge Univ. Press, 1932.
606 De Lange, W. P. and Healy, T. R.: New Zealand tsunamis 1840–1982, *New Zeal. J. Geol. Geophys.*,
607 29, 115–134, <https://doi.org/10.1080/00288306.1986.10427527>, 1986.
608 Lin, J., Rajesh, P. K., Lin, C. C. H., Chou, M., Liu, J.-Y., Yue, J., Hsiao, T.-Y., Tsai, H.-F., Chao, H.-
609 M., and Kung, M.-M.: Rapid Conjugate Appearance of the Giant Ionospheric Lamb Wave Signatures
610 in the Northern Hemisphere After Hunga- Tonga Volcano Eruptions, *Geophys. Res. Lett.*, 49,
611 e2022GL098222, <https://doi.org/10.1029/2022GL098222>, 2022.
612 Liu, P. L.-F. and Higuera, P.: Water waves generated by moving atmospheric pressure : Theoretical
613 analyses with applications to the 2022 Tonga event, *arXiv Prepr.*,
614 <https://doi.org/10.48550/arXiv.2205.05856>, 2022.
615 Liu, X., Xu, J., Yue, J., and Kogure, M.: Strong Gravity Waves Associated With Tonga Volcano
616 Eruption Revealed by SABER Observations, *Geophys. Res. Lett.*, 49, e2022GL098339,
617 <https://doi.org/10.1029/2022GL098339>, 2022.
618 Lynett, P., McCann, M., Zhou, Z., Renteria, W., Borrero, J., Greer, D., Fa’anunu, ‘Ofa, Bosserelle, C.,
619 Jaffe, B., Selle, S. La, Ritchie, A., Snyder, A., Nasr, B., Bott, J., Graehl, N., Synolakis, C., Ebrahimi,
620 B., and Cinar, G. E.: Diverse tsunamigenesis triggered by the Hunga Tonga-Hunga Ha’apai eruption,
621 *Nature*, 609, 728–733, <https://doi.org/10.1038/s41586-022-05170-6>, 2022.
622 Matoza, R. S., Matoza, R. S., Fee, D., Assink, J. D., Iezzi, A. M., Green, D. N., Kim, K., Lecocq, T.,
623 Krishnamoorthy, S., Lalande, J., Nishida, K., and Gee, K. L.: Atmospheric waves and global
624 seismoacoustic observations of the January 2022 Hunga eruption ,Tonga, *Science* (80- .),
625 <https://doi.org/10.1126/science.abo7063>, 2022.
626 Mori, N., Takahashi, T., Yasuda, T., and Yanagisawa, H.: Survey of 2011 Tohoku earthquake tsunami
627 inundation and run-up, *Geophys. Res. Lett.*, 38, L00G14, <https://doi.org/10.1029/2011GL049210>,
628 2011.
629 NASA: National Aeronautics and Space Administration,“Dramatic changes at Hunga Tonga-Hunga

630 Ha'apai," 2022.

631 Nomanbhoy, N. and Satake, K.: Generation mechanism of tsunamis from the 1883 Krakatau Eruption,
632 *Geophys. Res. Lett.*, 22, 509–512, <https://doi.org/10.1029/94GL03219>, 1995.

633 Omira, R., Baptista, M. A., Quartau, R., Ramalho, R. S., Kim, J., Ramalho, I., and Rodrigues, A.: How
634 hazardous are tsunamis triggered by small-scale mass-wasting events on volcanic islands ? New
635 insights from Madeira–NE Atlantic, *Earth Planet. Sci. Lett.*, 578, 117333,
636 <https://doi.org/10.1016/j.epsl.2021.117333>, 2022.

637 Otsuka, S.: Visualizing Lamb Waves From a Volcanic Eruption Using Meteorological Satellite
638 Himawari-8, *Geophys. Res. Lett.*, 49, e2022GL098324, <https://doi.org/10.1029/2022GL098324>, 2022.

639 Pelinovsky, E., Choi, B. H., Stromkov, A., Didenkulova, I., and Kim, H.: Analysis of Tide-Gauge
640 Records of the 1883 Krakatau Tsunami. In: Satake, K. (eds) *Tsunamis, Adv. Nat. Technol. Hazards*
641 *Res.*, 23, Springer, Dordrech, https://doi.org/10.1007/1-4020-3331-1_4, 2005.

642 Le Pichon, A., Blanc, E., and Hauchecorne, A.: Infrasound monitoring for atmospheric studies,
643 *Springer Science & Business Media*, 1–735 pp., <https://doi.org/10.1007/978-1-4020-9508-5>, 2010.

644 Plank, S., Marchese, F., Genzano, N., Nolde, M., and Martinis, S.: The short life of the volcanic island
645 New Late'iki (Tonga) analyzed by multi-sensor remote sensing data, *Sci. Rep.*, 10, 22293,
646 <https://doi.org/10.1038/s41598-020-79261-7>, 2020.

647 Rabinovich, A. B.: Spectral analysis of tsunami waves: Separation of source and topography effects, *J.*
648 *Geophys. Res. Ocean.*, 102, 12663–12676, <https://doi.org/10.1029/97JC00479>, 1997.

649 Rabinovich, A. B.: Seiches and harbor oscillations. in: *Handbook of coastal and ocean engineering*, pp.
650 193–236, 2009.

651 Rabinovich, A. B., Thomson, Æ. R. E., and Stephenson, F. E.: The Sumatra tsunami of 26 December
652 2004 as observed in the North Pacific and North Atlantic oceans, *Surv. Geophys.*, 27, 647–677,
653 <https://doi.org/10.1007/s10712-006-9000-9>, 2006.

654 Rabinovich, A. B., Titov, V. V., Moore, C. W., and Eble, M. C.: The 2004 Sumatra Tsunami in the
655 Southeastern Pacific Ocean: New Global Insight From Observations and Modeling, *J. Geophys. Res.*
656 *Ocean.*, 122, 7992–8019, <https://doi.org/https://doi.org/10.1002/2017JC013078>, 2017.

657 Ramalho, R. S., Winckler, G., Madeira, J., Helffrich, G. R., Hipólito, A., Quartau, R., Adena, K., and
658 Schaefer, J. M.: Hazard potential of volcanic flank collapses raised by new megatsunami evidence, *Sci.*

659 Adv., 1, e1500456, <https://doi.org/10.1126/sciadv.1500456>, 2015.

660 Ramírez-Herrera, M. T., Coca, O., and Vargas-Espinosa, V.: Tsunami Effects on the Coast of Mexico
661 by the Hunga Tonga-Hunga Ha'apai Volcano, *Pure Appl. Geophys.*, [https://doi.org/10.1007/s00024-](https://doi.org/10.1007/s00024-022-03017-9)
662 [022-03017-9](https://doi.org/10.1007/s00024-022-03017-9), 2022.

663 Satake, K.: Earthquakes: Double trouble at Tonga, *Nature*, 466, 931–932,
664 <https://doi.org/10.1038/466931a>, 2010.

665 Satake, K., Heidarzadeh, M., Quiroz, M., and Cienfuegos, R.: History and features of trans-oceanic
666 tsunamis and implications for paleo-tsunami studies, *Earth-Science Rev.*, 202, 103112,
667 <https://doi.org/10.1016/j.earscirev.2020.103112>, 2020.

668 Self, S. and Rampino, M. R.: K-1981Self_Nature_The 1883 eruption of Krakatau, *Nature*, 294, 699–
669 704, <https://doi.org/10.1038/294699a0>, 1981.

670 Stern, S., Cronin, S., Ribo, M., Barker, S., Brenna, M., Smith, I. E. M., Ford, M., Kula, T., and
671 Vaiomounga, R.: Post-2015 caldera morphology of the Hunga Tonga-Hunga Ha 'apai caldera ,
672 Tonga , through drone photogrammetry and summit area bathymetry, *EGU Gen. Assem.* 2022,
673 <https://doi.org/10.5194/egusphere-egu22-13586>, 2022.

674 Themens, D. R., Watson, C., Žagar, N., Vasylykevych, S., Elvidge, S., McCaffrey, A., Prikryl, P., Reid,
675 B., Wood, A., and Jayachandran, P. T.: Global Propagation of Ionospheric Disturbances Associated
676 With the 2022 Tonga Volcanic Eruption, *Geophys. Res. Lett.*, 49, e2022GL098158,
677 <https://doi.org/10.1029/2022GL098158>, 2022.

678 Thomson, R. E. and Emery, W. J.: *Data Analysis Methods in Physical Oceanography: Third Edition*,
679 New York: Elsevier, 1–716 pp., 2014.

680 Titov, V., Rabinovich, A. B., Mofjeld, H. O., Thomson, R. E., and Gonza, F. I.: The Global Reach of
681 the 26 December 2004 Sumatra Tsunami, *Science (80-.)*, 309, 2045–2049,
682 <https://doi.org/10.1126/science.1114576>, 2005.

683 USGS: M 5.8 Volcanic Eruption - 68 km NNW of Nuku'alofa, Tonga, *U.S. Geol. Surv.*, 2022.

684 Wang, Y., Heidarzadeh, M., Satake, K., Mulia, I. E., and Yamada, M.: A Tsunami Warning System
685 Based on Offshore Bottom Pressure Gauges and Data Assimilation for Crete Island in the Eastern
686 Mediterranean Basin, *J. Geophys. Res. Solid Earth*, 125, e2020JB020293,
687 <https://doi.org/10.1029/2020JB020293>, 2020.

688 Wang, Y., Zamora, N., Quiroz, M., Satake, K., and Cienfuegos, R.: Tsunami Resonance
689 Characterization in Japan Due to Trans-Pacific Sources: Response on the Bay and Continental Shelf, *J.*
690 *Geophys. Res. Ocean.*, 126, 1–16, <https://doi.org/10.1029/2020JC017037>, 2021.

691 Wang, Y., Heidarzadeh, M., Satake, K., and Hu, G.: Characteristics of two tsunamis generated by
692 successive Mw 7.4 and Mw 8.1 earthquakes in Kermadec Islands on March 4, 2021, *Nat. Hazards Earth*
693 *Syst. Sci.*, 22, 1–10, <https://doi.org/10.5194/nhess-2021-369>, 2022.

694 Watanabe, S., Hamilton, K., Sakazaki, T., and Nakano, M.: First Detection of the Pekeris Internal
695 Global Atmospheric Resonance: Evidence from the 2022 Tonga Eruption and from Global Reanalysis
696 Data, *J. Atmos. Sci.*, 79, 3027–3043, <https://doi.org/10.1175/jas-d-22-0078.1>, 2022.

697 Yuen, D. A., Scruggs, M. A., Spera, F. J., Yingcai Zheng, Hao Hu, McNutt, S. R., Glenn Thompson,
698 Mandli, K., Keller, B. R., Wei, S. S., Peng, Z., Zhou, Z., Mulargia, F., and Tanioka, Y.: Under the
699 Surface: Pressure-Induced Planetary-Scale Waves, Volcanic Lightning, and Gaseous Clouds Caused by
700 the Submarine Eruption of Hunga Tonga-Hunga Ha’apai Volcano Provide an Excellent Research
701 Opportunity, *Earthq. Res. Adv.*, <https://doi.org/10.1016/j.eqrea.2022.100134>, 2022.

702 Zhang, S., Vierinen, J., Aa, E., Goncharenko, L. P., Erickson, P. J., Rideout, W., Coster, A. J., and
703 Spicher, A.: 2022 Tonga Volcanic Eruption Induced Global Propagation of Ionospheric Disturbances
704 via Lamb Waves, *Front. Astron. Sp. Sci.*, 9, 1–10, <https://doi.org/10.3389/fspas.2022.871275>, 2022.

705